JACS
JOURNAL OF THE AMERICAN CHEMICAL SOCIETY
Article
pubs.acs.org/JACS

Solid Solution Alloy Nanoparticles of Immiscible Pd and Ru Elements Neighboring on Rh: Changeover of the Thermodynamic Behavior for Hydrogen Storage and Enhanced CO-Oxidizing Ability

Kohei Kusada,[*,†] Hirokazu Kobayashi,[†,‡] Ryuichi Ikeda,[†] Yoshiki Kubota,[§] Masaki Takata,[◇,◆] Shoichi Toh,[‡,∥] Tomokazu Yamamoto,[‡,∥] Syo Matsumura,[‡,∥] Naoya Sumi,[‡,⊥] Katsutoshi Sato,[‡,⊥,¶,⊗] Katsutoshi Nagaoka,[‡,⊥] and Hiroshi Kitagawa[*,†,‡,#,▽]

[†]Division of Chemistry, Graduate School of Science, Kyoto University, Kitashirakawa Oiwake-cho, Sakyo-ku, Kyoto 606-8502, Japan

[‡]Core Research for Evolutional Science and Technology (CREST), Japan Science and Technology Agency (JST), 7, Gobancho, Chiyoda-ku, Tokyo, 102-0076 Japan

[§]Department of Physical Science, Graduate School of Science, Osaka Prefecture University, 1-1 Gakuen-cho, Naka-ku, Sakai, Osaka 599-8531, Japan

[◇]RIKEN SPring-8 Center, 1-1-1 Kouto, Sayo-cho, Sayo-gun, Hyogo 679-5148, Japan

[◆]Japan Synchrotron Radiation Research Institute, 1-1-1 Kouto, Sayo-cho, Sayo-gun, Hyogo 679-5198, Japan

[∥]Research Laboratory for High Voltage Electron Microscopy, Kyushu University, 744 Motooka, Nishi-ku, Fukuoka, 819-0395, Japan

[⊥]Department of Applied Chemistry, Faculty of Engineering, Oita University, 700 Dannoharu, Oita 870−1192, Japan

[¶]Energy Technology Research Institute, National Institute of Advanced Industrial Science and Technology (AIST) 1-1-1 Umezono, Tsukuba, Ibaraki, 305-8568, Japan

[#]Institute for Integrated Cell-Material Sciences (iCeMS), Kyoto University, Yoshida, Sakyo-ku, Kyoto 606-8501, Japan

[▽]INAMORI Frontier Research Center, Kyushu University, 744 Motooka, Nishi-ku, Fukuoka 819-3095, Japan

Supporting Information

ABSTRACT: Pd_xRu_{1-x} solid solution alloy nanoparticles were successfully synthesized over the whole composition range through a chemical reduction method, although Ru and Pd are immiscible at the atomic level in the bulk state. From the XRD measurement, it was found that the dominant structure of Pd_xRu_{1-x} changes from fcc to hcp with increasing Ru content. The structures of Pd_xRu_{1-x} nanoparticles in the Pd composition range of 30−70% consisted of both solid solution fcc and hcp structures, and both phases coexist in a single particle. In addition, the reaction of hydrogen with the Pd_xRu_{1-x} nanoparticles changed from exothermic to endothermic as the Ru content increased. Furthermore, the prepared Pd_xRu_{1-x} nanoparticles demonstrated enhanced CO-oxidizing catalytic activity; $Pd_{0.5}Ru_{0.5}$ nanoparticles exhibit the highest catalytic activity. This activity is much higher than that of the practically used CO-oxidizing catalyst Ru and that of the neighboring Rh, between Ru and Pd.

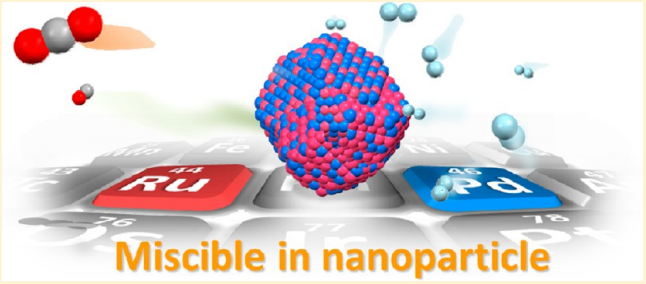

INTRODUCTION

Ru, Rh, and Pd are neighboring noble metals in the 4d transition metal series. No combination of binary alloy from these elements (Ru−Rh, Rh−Pd, and Ru−Pd) forms a solid solution alloy throughout the whole composition range at room temperature.[1] Here, we have succeeded for the first time in mixing Ru and Pd, which are the elements neighboring Rh, at the atomic level over the whole composition range using chemical reduction. Solid solution alloying has the advantage of allowing researchers to discover new properties by changing compositions or combinations of the constituent elements. For example, although Rh and Ag have no hydrogen storage ability, $Ag_{0.5}Rh_{0.5}$ solid solution nanoparticles exhibit a hydrogen storage property like Pd, which is located between Rh and Ag in the periodic table.[2] In this report, we focus on the hydrogen storage and CO-oxidizing abilities as the first property investigation for PdRu solid solution alloy nanoparticles. As a result, the hydrogen storage property of the alloy can be tuned by controlling the composition of Pd and Ru. More noteworthy is that the CO-oxidizing ability of the alloy is enhanced compared with that of Ru, Rh, and Pd monometallic nanoparticles.

Received: September 12, 2013
Published: January 23, 2014

dx.doi.org/10.1021/ja409464g | J. Am. Chem. Soc. 2014, 136, 1864−1871

Palladium is well-known as a hydrogen storage metal that absorbs hydrogen at ambient temperature and pressure.[3] Many bulk metals have been investigated as hydrogen storage materials, and it was found that their hydrogen storage properties are strongly correlated with their electronic structure.[4] To control the hydrogen storage properties, the influence of alloying with other metals, especially adjacent 4d metals in the periodic table, on the absorption properties has been intensively studied;[5] however, there are only a few reports on hydrogen storage properties in the Pd−Ru system, despite Ru's being the second-nearest 4d neighbor to Pd in the periodic table.[6]

On the other hand, Ru and Rh are well-known as good catalysts; for example, they are used as CO oxidation or NO_x reduction catalysts.[7] Recently, CO oxidation catalysts have been extensively developed because of their importance to CO removal from car exhaust or fuel-cell systems.[8] Pd, also well-known as a valuable catalyst, is used as a catalyst for fuel-cell electrodes and exhaust-gas purification;[9] however, these Pd catalysts crucially suffer from CO poisoning, which reduces catalytic activity,[10] and therefore, CO removal from the system is indispensable for long-term durability. Moreover, steam-reforming of shale gas is a popular source of synthesis gas for the generation of various chemical products and is strongly expected to be an important energy source in the near future. Recently, Ru has also attracted much attention as an effective catalyst for the steam-reforming reaction of methane, which is the main component of shale gas.[11] Furthermore, the catalytic properties of these platinum group elements are often enhanced by alloying with other elements.[12] Therefore, the Pd−Ru system is a promising candidate for innovative catalysts.

In addition, the 1:1 PdRu alloy is expected to possess an electronic structure similar to that of Rh because Rh is located between Ru and Pd in the periodic table. Although Rh has extremely high catalytic activity, it is one of the rarest and most expensive elements. Compared with Rh, Ru and Pd are much cheaper elements, and therefore, PdRu alloy is a useful material from the viewpoint of the "Element Strategy".[13] However, there have been very few reports of PdRu solid solution alloy so far. The reason originates from the fact that Pd−Ru solid solution alloy cannot be easily obtained. Pd and Ru are immiscible at the atomic level throughout the whole composition range in the bulk state, even at high temperatures up to the melting point of Pd.[1c] To obtain the PdRu solid solution alloys throughout the whole composition range, we focused on metal nanoparticles. Recently, the nanosize effect has attracted much attention not only for developing potential applications for electronic, magnetic, optical, and catalytic materials but also for providing an efficient technique for stabilizing a nonequilibrium phase under ambient conditions.[14]

EXPERIMENTAL SECTION

Synthesis of Pd_xRu_{1-x} Nanoparticles. In a typical synthesis of Pd_xRu_{1-x} nanoparticles (x = 0.5), poly(*N*-vinyl-2-pyrrolidone) (PVP, 444 mg, MW ≈ 40 000, Wako) was dissolved in triethylene glycol (TEG, 100 mL, Wako), and the solution was heated to 200 °C in air with magnetic stirring. Meanwhile, $K_2[PdCl_4]$ (163.4 mg, Aldrich) and $RuCl_3 \cdot nH_2O$ (131.1 mg, Wako) were dissolved in deionized water (40 mL). The aqueous mixture solution was then slowly added to the TEG solution. The solution was maintained at 200 °C while adding the solution. After cooling to room temperature, the prepared nanoparticles were separated by centrifuging. Other Pd_xRu_{1-x} (x = 0.1, 0.3, 0.7, and 0.9) nanoparticles were prepared by controlling the molar ratio of Pd^{2+} and Ru^{3+} ions. The details of the synthesis conditions for Pd_xRu_{1-x} nanoparticles are summarized in Supporting Information Table S1.

Characterization. The atomic ratios of Pd and Ru in nanoparticles were determined using energy-dispersive X-ray (EDX) techniques. Transmission electron microscopy (TEM) images were taken using a Hitachi HT7700 operated at 100 kV. High-resolution (HR) TEM, selected area diffraction pattern (SADP), and dark field (DF) TEM images were captured using a JEOL JEM-3200FSK TEM instrument operated at 300 kV. High-resolution scanning transmission electron microscopy (HRSTEM), high-angle annular dark-field (HAADF)-STEM and EDX analyses were recorded on a Hitachi HD-2700 STEM instrument operated at 200 kV at the Naka Application Center, Hitachi High-Technologies Corporation and a JEM-ARM 200F STEM instrument operated at 200 kV. Synchrotron X-ray diffraction (XRD) patterns were measured at the BL02B2 beamline, SPring-8. Pressure−composition (PC) isotherms were measured using a pressure−composition−temperature apparatus (Suzuki Shokan Co., Ltd.). Solid-state ^2H NMR spectra were measured at 303 K in a fixed magnetic field of 94 kOe using a Bruker AVANCE II NMR spectrometer. The ^2H shift values were determined by use of the internal ^2H gas signal. X-ray photoelectron spectroscopy (XPS) spectra were recorded on a Shimadzu ESCA-3400 X-ray photoelectron spectrometer.

Catalyst Preparation. To investigate the CO-oxidizing catalytic activities, Ru, Rh, Pd, and Pd_xRu_{1-x} alloy nanoparticles and a physical mixture (Ru and Pd nanoparticles) supported on γ-Al_2O_3 catalysts were prepared by wet impregnation. Each nanoparticle (equivalent to 1 wt % of γ-Al_2O_3) was ultrasonically dispersed in purified water. γ-Al_2O_3 support that had been precalcined at 1073 K for 5 h was put into each aqueous solution of nanoparticles, and then the suspended solutions were stirred for 12 h. After stirring, the suspended solutions were heated to 60 °C and dried under vacuum. The resulting powders were kept at 120 °C for 8 h to remove water completely.

Catalytic Tests. The obtained catalyst powders were pressed into pellets at 1.2 MPa for 5 min. The pellets were crushed and sieved to obtain grains with diameters between 180 and 250 μm. Each supported nanoparticle catalyst (150 mg) was loaded into a tubular quartz reactor (i.d. 7 mm) with quartz wool. CO/O_2/He mixed gas ($He/CO/O_2$: 49/0.5/0.5 mL min^{-1}) was passed over the catalysts at ambient temperature, and the catalysts were then heated to 100 °C. After 15 min, effluent gas was collected, and the reaction products were analyzed by gas chromatography with a thermal conductivity detector (GC-8A, Shimadzu, Japan). Catalysts were heated in increments of 10 °C to a temperature at which CO was consumed completely, and the products were analyzed at each temperature.

RESULTS AND DISCUSSION

To investigate the composition of Pd and Ru atoms in the prepared nanoparticles, elemental analyses were carried out using EDX techniques. The average stoichiometries determined from the EDX data are summarized in Supporting Information Table S2 and Figure S1.

TEM images of the synthesized Pd_xRu_{1-x} nanoparticles were recorded on a Hitachi HT7700 TEM instrument (Figure 1). The mean diameters of the nanoparticles were determined from the TEM images to be (a) 6.4 ± 1.7, (b) 9.4 ± 1.7, (c) 12.5 ± 2.2, (d) 10.0 ± 1.2, (e) 8.2 ± 1.6, (f) 8.6 ± 1.4, and (g) 9.8 ± 2.6 nm, respectively. These mean diameters were estimated by averaging over at least 300 particles. Nonspherical nanoparticles were observed in Ru-rich nanoparticles; this is considered to arise from the nature of hcp-structured Ru with an anisotropic growth direction as shown in Figure 1a.

First of all, to clarify the structure of the prepared PdRu nanoparticles, $Pd_{0.5}Ru_{0.5}$ nanoparticles were investigated in detail. Figure 2 shows elemental mapping data for the prepared $Pd_{0.5}Ru_{0.5}$ nanoparticles. Figure 2a is a HAADF-STEM image. Parts b and c of Figure 2 are the corresponding Pd-L and Ru-L

dx.doi.org/10.1021/ja409464g | J. Am. Chem. Soc. 2014, 136, 1864−1871

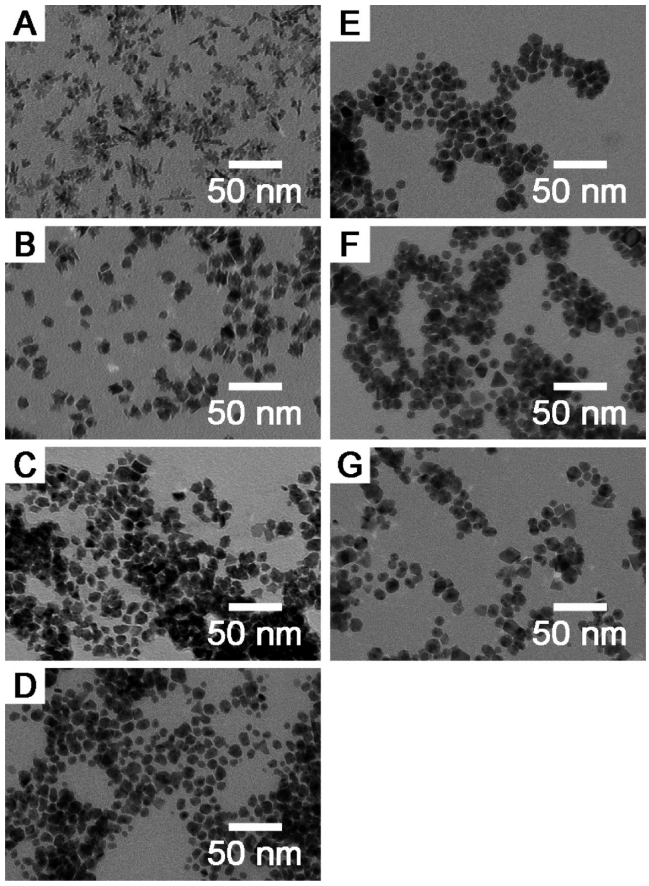

Figure 1. The TEM images of (a) Ru, (b) $Pd_{0.1}Ru_{0.9}$, (c) $Pd_{0.3}Ru_{0.7}$, (d) $Pd_{0.5}Ru_{0.5}$, (e) $Pd_{0.7}Ru_{0.3}$, (f) $Pd_{0.9}Ru_{0.1}$, and (g) Pd nanoparticles.

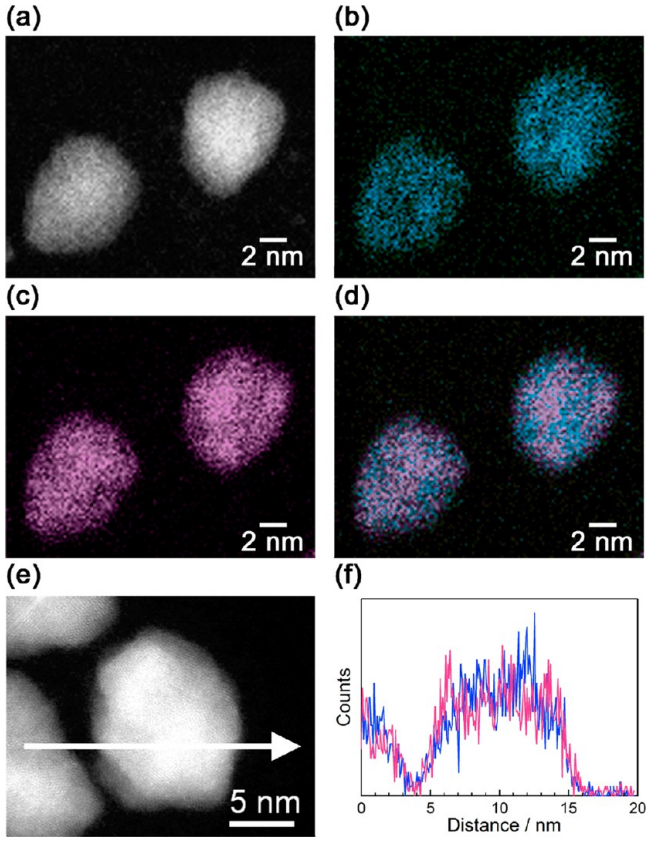

Figure 2. (a) HAADF-STEM image, (b) Pd-L STEM–EDX map and (c) Ru-L STEM–EDX map obtained for a group of prepared $Pd_{0.5}Ru_{0.5}$ nanoparticles. (d) Reconstructed overlay image of the maps shown in panels b and c (blue, Pd; red, Ru). (f) Compositional line profiles of Pd (blue) and Ru (red) for the $Pd_{0.5}Ru_{0.5}$ nanoparticle recorded along the arrow shown in the STEM image (e).

STEM–EDX maps, respectively. Figure 2d is an overlay map of the Pd and Ru chemical distributions. The map provides visual evidence for the formation of $Pd_{0.5}Ru_{0.5}$ solid solutions. We further characterized the $Pd_{0.5}Ru_{0.5}$ nanoparticles by EDX line scanning analysis (Figure 2e, f)). The line-scan position of the nanoparticle is denoted by the white arrow in Figure 2e. The compositional line profiles of Pd and Ru on a $Pd_{0.5}Ru_{0.5}$ nanoparticle show that Ru and Pd atoms are homogeneously distributed over the whole particle. These results indicate the formation of atomic-level PdRu alloy. Pd and Ru have different redox potentials; that is, Pd ions are easily reduced to Pd metal, as compared with Ru ions. If both Pd and Ru precursors are added to a TEG solution before heating, Pd ions are first reduced around 90 °C, and Ru ions are subsequently reduced around 160 °C by TEG, resulting in the formation of the segregated structure of Pd and Ru. The point of synthesis for solid-solution structure is to slowly add these metal precursors into thoroughly heated TEG solution to simultaneously reduce these metal ions to metals. In this report, the metal precursor solution was slowly added to TEG heated at 200 °C. The added metal solution turned black instantaneously, indicating that both metal ions are quickly reduced, and the difference in the reduction speed is considered to be negligible. As a consequence of the simultaneous reduction of Pd and Ru ions, we successfully synthesized the solid-solution structure nanoparticles.

The crystal structure of $Pd_{0.5}Ru_{0.5}$ nanoparticles was investigated by synchrotron XRD analysis at the beamline BL02B2, SPring-8. The diffraction patterns of samples sealed in glass capillaries under vacuum were measured at 303 K. Parts a and b of Figure 3 show the XRD patterns of Ru, Pd, and $Pd_{0.5}Ru_{0.5}$ nanoparticles. As shown in Figure 3a, Ru and Pd nanoparticles showed a powder XRD pattern originating from a single hexagonal close-packed (hcp) and face-centered cubic (fcc) lattice, respectively, as well as those bulks. By contrast, $Pd_{0.5}Ru_{0.5}$ nanoparticles have an XRD pattern comprising two components diffracted from fcc and hcp lattices, where the positions of the diffraction peaks differ from those of Ru (hcp) or Pd (fcc) monometallic nanoparticles (Figure 3b). From the Rietveld refinement of the diffraction pattern for $Pd_{0.5}Ru_{0.5}$ nanoparticles, the lattice constants for the two components were refined to be a = 3.852(1) Å for the fcc lattice and a = 2.7227(8) Å and c = 4.381(2) Å for the hcp lattice (Figure 3c). The lattice constant of the fcc component is smaller than that of Pd (a = 3.8925 Å), and the lattice constants of the hcp components are larger than those of Ru (a = 2.7054 Å, c = 4.2788 Å). These results strongly support the formation, in both fcc and hcp phases, of atomic-level $Pd_{0.5}Ru_{0.5}$ alloys.

The structure of solid solution $Pd_{0.5}Ru_{0.5}$ nanoparticles was further characterized by using TEM; that is, we determined whether fcc and hcp phases exist separately as individual nanoparticles or coexist in a single nanoparticle. Figure 4a shows a bright field (BF) TEM image of a $Pd_{0.5}Ru_{0.5}$ nanoparticle. The nanoparticle is polycrystalline with small grains. Part b is the SADP of the $Pd_{0.5}Ru_{0.5}$ nanoparticle in part a. The d spacings from diffraction spots A and B were calculated

dx.doi.org/10.1021/ja409464g | J. Am. Chem. Soc. 2014, 136, 1864–1871

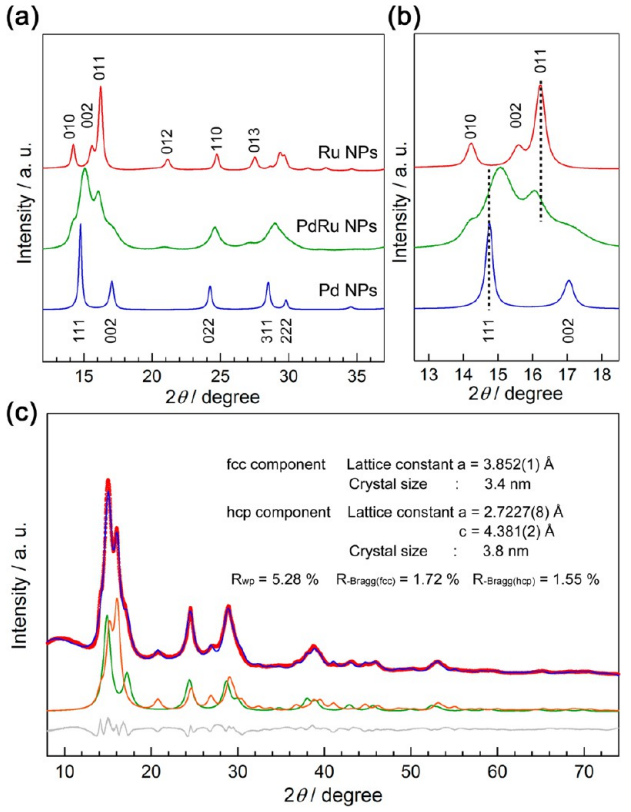

Figure 3. (a) Synchrotron XRD patterns (2θ = 12°−37°) of Ru, Pd, and $Pd_{0.5}Ru_{0.5}$ nanoparticles at 303 K. (b) Close-up of the 2θ = 12.5°−19° region. (c) The diffraction pattern of $Pd_{0.5}Ru_{0.5}$ nanoparticles (red circles) at 303 K and the calculated pattern (blue line). The bottom lines show the difference profile (gray) and the fitting curves of the fcc component (green) and hcp component (orange). The radiation wavelength was 0.57803(2) Å.

to be 2.24 and 1.69 Å, respectively. Taking into account *d* values obtained from the XRD pattern, the diffraction spots of A and B correspond to fcc (111) (*d* spacing of 2.24 Å) and hcp (012) (*d* spacing of 1.61 Å) lattices, respectively. Parts c and d of Figure 4 are DFTEM images obtained for diffraction spots A and B, respectively. Parts c and d show fcc (111) and hcp (012) grains, respectively, and it is seen that each grain is located in a different position. Taking the results of the STEM−EDX map, XRD patterns, and DFTEM image into consideration, it was clearly demonstrated that the solid solution fcc and solid solution hcp phases coexist in a single $Pd_{0.5}Ru_{0.5}$ nanoparticle.

Nanoparticles of the other compositions were also investigated by similar methods, including elemental mapping and XRD measurements. Supporting Information Figure S2 shows elemental mapping data for the prepared Pd_xRu_{1-x} nanoparticles. Supporting Information Figures S2(A), (C), (E) and (G) are HAADF−STEM images of Pd_xRu_{1-x} nanoparticles. Supporting Information Figures S2(B), (D), (F) and (H) are the overlay maps of the corresponding Pd−L (blue) and Ru−L (red) STEM−EDX maps of Pd_xRu_{1-x} nanoparticles. These maps provide visual evidence for the formation of Pd_xRu_{1-x} solid solutions.

The crystal structures of Pd_xRu_{1-x} bimetallic nanoparticles were also investigated by synchrotron XRD at the beamline BL02B2, SPring-8, as with $Pd_{0.5}Ru_{0.5}$ nanoparticles. Figure 5a shows the XRD patterns of the Pd and Ru, and Pd_xRu_{1-x} nanoparticles. The dominant diffraction pattern of Pd_xRu_{1-x}

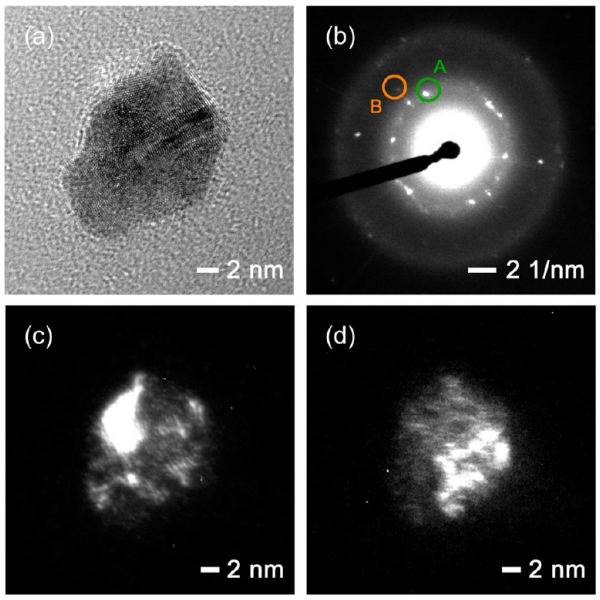

Figure 4. (a) BFTEM image of a $Pd_{0.5}Ru_{0.5}$ nanoparticle, (b) SADP of part a, (c) DFTEM image of a $Pd_{0.5}Ru_{0.5}$ nanoparticle. Part of the fcc(111) diffraction spots was selected as the image-forming diffraction vector, as indicated schematically by A (green circle) in part b. (d) DFTEM image of a $Pd_{0.5}Ru_{0.5}$ nanoparticle. Part of the hcp(012) diffraction spots was selected as the image-forming diffraction vector, as indicated schematically by B (orange circle) in part b.

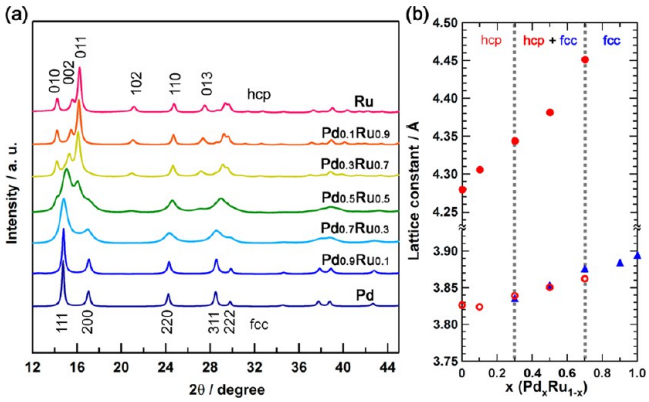

Figure 5. (a) The synchrotron XRD patterns (2θ = 12−45°) of Pd_xRu_{1-x} nanoparticles at 303 K. The radiation wavelength was 0.57803(2) Å. (b) The dependence of the lattice constant on the metal composition in Pd_xRu_{1-x} nanoparticles at 303 K. ○ (red), the lattice constant *a* of the hcp component; ● (red), the lattice constant *c* of the hcp component; ▲ (blue), the lattice constant of the fcc component.

nanoparticles changes from the fcc pattern to the hcp pattern with increasing Ru content in the PdRu nanoparticles. The crystal structures of Pd_xRu_{1-x} were also determined by the Rietveld refinement. The refinement results are summarized in Supporting Information Figure S3. From the refinement results, the structures of Pd_xRu_{1-x} nanoparticles ($0.3 \leq x \leq 0.7$) consisted of both fcc and hcp structures.

Figure 5b shows the lattice constants of Pd_xRu_{1-x} nanoparticles estimated from the Rietveld refinements of the XRD patterns. Because both of the fcc and hcp structures are close-packed structures, the square root of the lattice constant *a* in the hcp component is in accordance with the lattice parameter *a* in the fcc component. As shown in Figure 5b, the lattice constants increased linearly with increasing Pd content (x). The

dx.doi.org/10.1021/ja409464g | J. Am. Chem. Soc. 2014, 136, 1864−1871

linear correlation between the lattice constant and the alloy composition follows Vegard's law, which is an approximate empirical rule proposing a linear relation, at constant temperature, between the crystal lattice constant of an alloy and the concentrations of the constituent elements.[15] Furthermore, in the Pd composition range of 30−70%, the lattice constants a in fcc and the square root of the lattice constant a in hcp components at the same metal composition have almost the same value. This result means that the metal compositions in coexisting fcc and hcp phases have almost the same values, and these values correspond to the average stoichiometry determined from the EDX data. These results strongly support the formation of the atomic-level PdRu alloy over the whole composition range.

Studies on hydrogen-absorption properties of the metal nanoparticles give important information related to the structure and the electronic state.[4] To investigate the hydrogen-absorption properties accompanied by the addition of Ru atoms to Pd nanoparticles, PC isotherms of Pd_xRu_{1-x} nanoparticles were measured at 303 K. As shown in Figure 6,

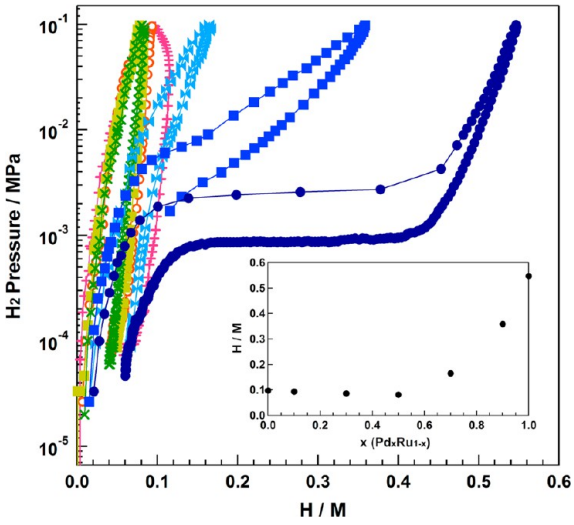

Figure 6. The PC isotherms of Pd_xRu_{1-x} nanoparticles (dark blue, Pd; blue, $Pd_{0.9}Ru_{0.1}$; light blue, $Pd_{0.7}Ru_{0.3}$; green, $Pd_{0.5}Ru_{0.5}$; yellow, $Pd_{0.3}Ru_{0.7}$; orange, $Pd_{0.1}Ru_{0.9}$; pink, Ru at 303 K). Inset is the metal composition dependence of the hydrogen storage capacity in Pd_xRu_{1-x} nanoparticles.

the hydrogen concentration of Pd−Ru nanoparticles decreased with increasing Ru content: 30 atom % replacement of Pd with Ru results in a reduction of more than half of the total amount of hydrogen absorption at ∼100 kPa (0.2 H/$Pd_{0.7}Ru_{0.3}$). With the further addition of Ru atoms, the amount of absorbed hydrogen decreased to 0.1 H/M below x = 0.5 (Figure 6 inset). This drastic reduction in hydrogen absorption suggests a change in the thermodynamic behavior for hydrogen storage in PdRu nanoparticles with metal composition. It was confirmed that the solid-solution structure of Pd−Ru nanoparticles was maintained before and after hydrogen treatment (Figure S4).

Figure 7 shows the temperature dependence of PC isotherms in Pd_xRu_{1-x} nanoparticles. As shown in Figure 7a, Pd nanoparticles exhibited an exothermic reaction with hydrogen that was analogous to that of Pd bulk,[3] that is, Pd nanoparticles absorb hydrogen at 303 K more than at 423 K.

The reaction of hydrogen with $Pd_{0.9}Ru_{0.1}$ nanoparticles was also exothermic. The tendency of temperature dependence of

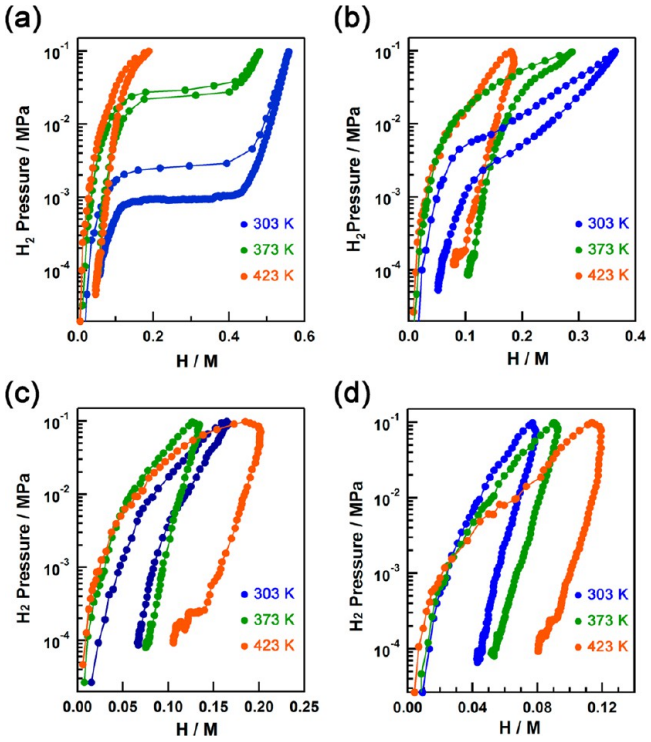

Figure 7. The temperature dependence of PC isotherms in (a) Pd, (b) $Pd_{0.9}Ru_{0.1}$, (c) $Pd_{0.7}Ru_{0.3}$, and (d) $Pd_{0.5}Ru_{0.5}$ nanoparticles.

PC isotherms further changes with metal composition, and finally, the $Pd_{0.5}Ru_{0.5}$ nanoparticles can absorb more hydrogen at 423 K than at 303 K. These results show that the enthalpy of hydrogen absorption for the Pd_xRu_{1-x} nanoparticles varied from exothermic to endothermic as the Ru content increased. This phenomenon might be caused by the change in electronic state of Pd with increasing Ru. The significance of this work is the success in continuously controlling the thermodynamic parameters for the reaction of Pd_xRu_{1-x} with hydrogen by atomic-level alloying.

To investigate the further hydrogen storage properties, the numerical values of the thermodynamic parameters of hydrogen absorption in Pd_xRu_{1-x} nanoparticles were estimated. In the hydrogen storage metals exhibiting an exothermic reaction with hydrogen, there are two phases through the reaction with hydrogen. One is the solid solution phase (α phase; M + H) of metals and hydrogen and the other is the hydride phase (β phase; M−H) with a metallic bond. The phase transition from the α phase to the β phase takes place with an accompanying plateau pressure in the PC isotherm. From Figure 6, plateau-like behavior was observed in PC isotherms of Pd, $Pd_{0.9}Ru_{0.1}$, and $Pd_{0.7}Ru_{0.3}$ nanoparticles. This implies that these three kinds of nanoparticles were transformed from the α phase to the β phase and the other nanoparticles remained in the α phase under a hydrogen pressure of 0.1 MPa. When the phase transition was treated as a chemical reaction, we obtained

$$\frac{2}{C_\beta - C_\alpha}\mathrm{MH}_{C_\alpha} + \mathrm{H}_2 = \frac{2}{C_\beta - C_\alpha}\mathrm{MH}_{C_\beta} + \Delta H_{\alpha\to\beta}$$

where $\Delta H_{\alpha\to\beta}$ is the heat of formation, C_α is the maximum hydrogen concentration in the α phase, and C_β is the minimum hydrogen concentration in the β phase.[16] C_α and C_β correspond to the start and end of the plateau region, respectively. As shown in Figure 6, a plateau-like region was observed in both

dx.doi.org/10.1021/ja409464g | J. Am. Chem. Soc. 2014, 136, 1864−1871

Pd and $Pd_{0.9}Ru_{0.1}$ nanoparticles. An equilibrium pressure in this region is correlated with the $\Delta H_{\alpha\to\beta}$ and the entropy change ($\Delta S_{\alpha\to\beta}$) for the phase transition from the α phase to the β phase. In the case that 1 mol of hydrogen gas is consumed in the reaction, the thermodynamics are described below,[17]

$$\ln \frac{P}{P_0} = \frac{\Delta H_{\alpha\to\beta}}{RT} - \frac{\Delta S_{\alpha\to\beta}}{R} \quad (1)$$

where P is the equilibrium hydrogen pressure and P_0 is the standard hydrogen pressure (0.1 MPa). $\Delta H_{\alpha\to\beta}$ and $\Delta S_{\alpha\to\beta}$ were calculated from eq 1 and the results are summarized in Supporting Information Table S3. Both $\Delta H_{\alpha\to\beta}$ and $\Delta S_{\alpha\to\beta}$ for Pd nanoparticles are larger than those of Pd bulk. Furthermore, those thermodynamic parameters increase with increasing Ru content. The $\Delta H_{\alpha\to\beta}$ is correlated with the bond strength between the metal and hydrogen in the β phase. As previously reported,[18] this result also shows that the Pd nanoparticles have a larger $\Delta H_{\alpha\to\beta}$ value than Pd bulk. This implies that the bond strength between Pd and H atoms becomes weaker with decreasing particle size. On the other hand, the $\Delta H_{\alpha\to\beta}$ value is remarkably increased in $Pd_{0.9}Ru_{0.1}$ nanoparticles. The more the Ru content increases, the weaker the bond strength of M−H in the alloy. This phenomenon suggests a change in the electronic states of metals because of the formation of a solid solution alloy.

The $\Delta S_{\alpha\to\beta}$ value of $Pd_{0.9}Ru_{0.1}$ nanoparticles is larger than that of Pd nanoparticles. The $\Delta S_{\alpha\to\beta}$ during the hydride formation comes mainly from the entropy loss of the hydrogen gas. The larger $\Delta S_{\alpha\to\beta}$ in $Pd_{0.9}Ru_{0.1}$ nanoparticles indicates that the hydrogen atoms possess a larger entropy compared with that in Pd nanoparticles. In other words, hydrogen atoms in the nanoparticles retain a part of the freedom in the gaseous state, implying that atomic arrangements or lattice defects in nanoparticles are statically or dynamically disordered because of the formation of a solid solution structure. From these results, we succeeded in controlling the hydrogen absorption properties and electronic structure of Pd_xRu_{1-x} nanoparticles by metal composition over the whole composition range.

Solid-state ^2H NMR measurements were performed to investigate the state of ^2H in the Pd_xRu_{1-x} nanoparticles (Figure 8). In the spectrum of Pd nanoparticles, a broad absorption line at 31 ppm and a sharp line around 0 ppm were observed. In the spectrum of $^2H_2$ gas, only a sharp line around 0 ppm was obtained. On comparison of these spectra, we can attribute the sharp line observed in the Pd nanoparticles to free deuterium gas ($^2H_2$) and the broad component to absorbed deuterium atoms (^2H) in the particles. Deuterium absorbed inside the lattice of Pd_xRu_{1-x} alloy nanoparticles also produced broad signals. Chemical shift values of the broad lines observed in Pd_xRu_{1-x} are summarized in Figure 8b. Pd hydride shows the lowest-field shift of the ^2H atoms. The d band in Pd hydride is almost filled,[3a] so the d spin correlation is weakened, and the Knight shift is the dominant factor in the NMR shift of ^2H in Pd hydride. In contrast, for a Pd content of 70 and 90 atom %, the observed lines are markedly shifted upfield. This shift can be explained by the ^2H s electron's being polarized by the d spin paramagnetism of the PdRu nanoparticles arising from the formation of a hydride (Pd−Ru−H). Because a large number of holes exist in the d band of Pd−Ru, the spin correlation between the conduction electrons of the Pd−Ru hydride is large enough to cause spin polarization in the ^2H s electrons in the Pd−Ru hydride. The marked decrease in the shift value upon adding Ru to Pd from x = 1.0 to 0.7 can be explained by the increase of the effect from the paramagnetic spins in the d band.

With the further addition of Ru atoms (under 50 atom %), the shift value of the broad absorption lines, originating from ^2H inside the Pd−Ru lattice, jumped to near 0 ppm and became almost independent of the metal composition. This sudden change observed at x = 0.5 corresponds to the changeover of thermodynamic behavior from exothermic to endothermic and destabilization of the hydride phase that were observed in the PC isotherms. From the present result of NMR shift values, we conclude that remarkable changes in the electronic structure of Pd_xRu_{1-x} take place at x = 0.5 and between x = 0.9 and 1.0.

To investigate the CO-oxidizing catalytic activity, prepared Pd_xRu_{1-x} alloy, Rh nanoparticles, and a physical mixture of Ru and Pd nanoparticles were supported on γ-Al_2O_3 using the wet impregnation method. Figure 9 compares the CO conversions for 1 wt % of each nanoparticle supported on γ-Al_2O_3. The temperatures corresponding to 50% conversion (T_{50}) of CO to CO_2 for $Pd_{0.5}Ru_{0.5}$, Ru, Rh, and Pd catalysts were ~125, 165, 165, and 195 °C, respectively. The temperatures for 100% conversion (T_{100}) of CO to CO_2 were 140, 170, 170, and 200 °C, respectively. From these results, it is clear that the

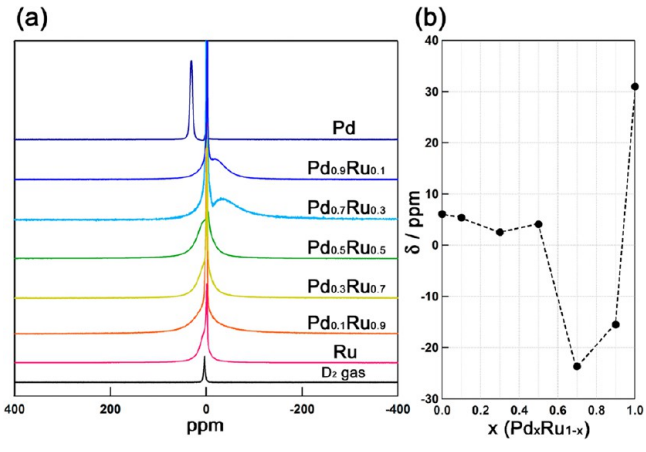

Figure 8. (a) The solid-state ^2H NMR spectra for Pd_xRu_{1-x} nanoparticles and $^2H_2$ gas. All of the samples were measured under 101.3 kPa of $^2H_2$ gas at 303 K. (b) The chemical shift position of the broad absorption lines in Pd_xRu_{1-x} nanoparticles.

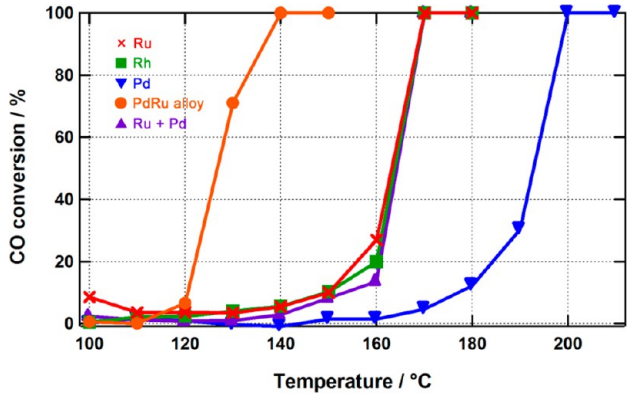

Figure 9. Temperature dependence of CO conversion in Ru (× red), Rh (■ green), Pd (▼ blue), $Pd_{0.5}Ru_{0.5}$ solid solution (● orange), and Ru + Pd mixture (▲ purple) nanoparticles supported on γ-Al_2O_3.

dx.doi.org/10.1021/ja409464g | J. Am. Chem. Soc. 2014, 136, 1864−1871

$Pd_{0.5}Ru_{0.5}$ nanoparticles have the highest activity for 50% and 100% conversions of CO to CO_2. $Pd_{0.5}Ru_{0.5}$ shows a 30−40 K lower conversion temperature compared with the most efficient CO-oxidation catalyst, Ru. In addition, the conversion temperature was lower than that for the most expensive precious metal, Rh. That is, $Pd_{0.5}Ru_{0.5}$ nanoparticles are more efficient CO-oxidation catalysts than Rh. On the other hand, the conversion property of the physical mixture of Ru and Pd nanoparticles differs totally from that of $Pd_{0.5}Ru_{0.5}$. The physical mixture of Ru and Pd nanoparticles shows the same conversion property as that of Ru nanoparticles because the Ru nanoparticle is better and dominant in the CO-oxidation reaction compared with the Pd nanoparticle. These results demonstrate a novel strategy to create functional materials on the basis of interelemental fusion. The extreme enhancement of the CO-oxidizing ability observed for $Pd_{0.5}Ru_{0.5}$ alloy is considered to originate from a new electronic state realized by the atomic-level alloying of Pd and Ru.

To investigate further the catalytic activity of Pd_xRu_{1-x} nanoparticles, the temperature dependence of CO conversion for each metal composition nanoparticle was measured. Figure 10 shows the metal-composition dependence of the CO

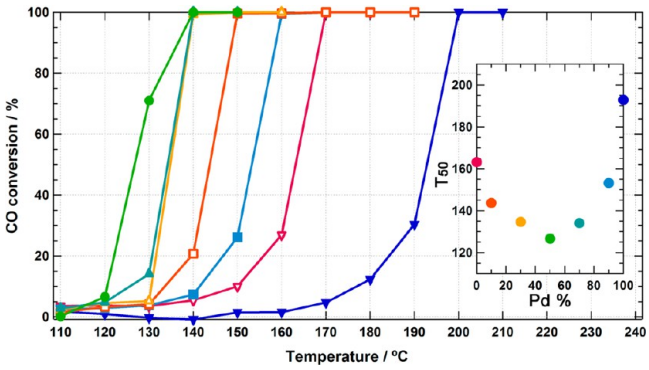

Figure 10. Temperature dependence of CO conversion in Pd_xRu_{1-x} nanoparticles supported on γ-Al_2O_3; x = 0 (▽ red), 0.1 (□ orange), 0.3 (△ yellow), 0.5 (● green), 0.7 (▲ blue-green), 0.9 (■ light blue), and 1.0 (▼ blue). The inset is the metal composition dependence of T_{50}.

conversion in Pd_xRu_{1-x} nanoparticles supported on γ-Al_2O_3. The T_{50} and T_{100} in all of the alloy nanoparticles are lower than those in pure Ru or Pd nanoparticles, and those temperatures reached a minimum at the ratio of Pd/Ru = 50:50. From these results, it is revealed that the $Pd_{0.5}Ru_{0.5}$ nanoparticles have the highest activity for 50% and 100% conversions of CO to CO_2. This kind of inverse volcano type behavior for CO oxidation has been reported in many types of alloy nanoparticle catalysts, such as Au−Pd[19] and Au−Ag.[20]

It has been reported that the CO-oxidation reaction takes place between chemisorbed species (Langmuir−Hinshelwood mechanism), and thus, O + CO coadsorption was considered as the initial states of the oxidation reaction.[21] The position of the d band center, relative to the Fermi level, is an important parameter controlling adsorption of O and CO or activation energy barriers for CO oxidation.[22] By the atomic-level alloying, the d band center of $Pd_{0.5}Ru_{0.5}$ is considered to change to a favorable condition for CO and O coverage or high reactivity of CO with O atoms on the bimetallic surface. In addition, it has been reported that defect sites can also significantly affect the catalytic activity.[23] The coexistence of both fcc and hcp domains in a Pd−Ru single particle is considered to generate defect structures with vacancies in the domain boundaries, leading to the high reactivity of CO with O atoms. A theoretical calculation to clarify the mechanism and the correlation between metal composition and the CO conversion for Pd_xRu_{1-x} nanoparticles is currently in progress.

Furthermore, we confirmed that the solid solution structure was maintained in the nanoparticles before and after the catalytic reaction (Supporting Information Figure S5). The novel PdRu nanostructured materials have not only high catalytic activity but also high durability for the CO-oxidation reaction.

The change in the electronic structure because of atomic-level alloying of Ru and Pd was investigated by XPS measurements (Supporting Information Figure S6, S7). The Pd 3d and Ru 3p binding energies are summarized in Supporting Information Table S4. The Pd 3d binding energies of the alloys shifted to higher energy with Ru content, which is in agreement with the oxidization of Pd. By contrast, the Ru 3p binding energies of the alloys shifted to lower energy with Pd content, which is in agreement with the reduction of Ru. Thus, the XPS spectra for Pd_xRu_{1-x} nanoparticles indicate that the electronic state of Pd_xRu_{1-x} nanoparticles differs from those of Ru and Pd nanoparticles and that electrons of Pd atoms slightly transfer to Ru atoms. This electron transfer may also be responsible for the catalytic enhancement, which would be consistent with d band theory suggested in previous reports.[22,24]

■ CONCLUSION

In summary, we first synthesized Pd_xRu_{1-x} solid solution alloy nanoparticles over the whole composition range through the chemical reduction method, although Ru and Pd are immiscible at the atomic level in the bulk state. From the XRD measurement, it was found that the structure of Pd_xRu_{1-x} changes from fcc to hcp with increasing Ru content. The structures of Pd_xRu_{1-x} nanoparticles in the Pd composition range of 30% to 70% consisted of both fcc and hcp structures, and both phases coexist in a single particle. We examined hydrogen storage properties and the CO-oxidizing reaction. The amount of hydrogen absorption depends on the composition of the alloy. The reaction of hydrogen with the Pd_xRu_{1-x} nanoparticles changed from exothermic to endothermic as the Ru content increased. Accordingly, this difference in the amounts of hydrogen absorption implies a difference in the electronic structures of the Pd_xRu_{1-x} nanoparticles. Furthermore, the prepared Pd_xRu_{1-x} nanoparticles exhibit enhanced CO-oxidizing catalytic activity; $Pd_{0.5}Ru_{0.5}$ nanoparticles showed the highest catalytic activity, and this activity is also higher than that of Rh. Our present work provides a novel strategy on the basis of interelemental fusion to create highly efficient functional materials for energy and material conversions.

■ ASSOCIATED CONTENT

Ⓢ Supporting Information

Reaction conditions for the syntheses of nanoparticles, the results of the metal composition, the HAADF-STEM images and elemental mapping data for the Pd_xRu_{1-x} nanoparticles, the results of Rietveld refinement, in situ XRD patterns, the calculated thermodynamic parameters, and the XPS spectra. This material is available free of charge via the Internet at http://pubs.acs.org.

AUTHOR INFORMATION

Corresponding Author

kusada@kuchem.kyoto-u.ac.jp; kitagawa@kuchem.kyoto-u.ac.jp

Present Address

[⊗]Elements Strategy Initiative for Catalysts and Batteries (ESICB), Kyoto University, 1-30 Goryo-Ohara, Nishikyo-ku, Kyoto 615-8245, Japan.

Notes

The authors declare no competing financial interest.

ACKNOWLEDGMENTS

We are thankful to T. Sato and Y. Suzuki at Hitachi High-Technologies Corporation Application Development Dept. for supporting STEM and EDX measurements. This work was supported in part by a Research Fellowship for Young Scientists (No. 22·3504) from the JSPS.

REFERENCES

(1) (a) Tripathi, S. N.; Bharadwaj, S. R.; Chandransekharaiah, M. S. *J. Phase Equilib.* **1996**, *17*, 362. (b) Massalski, T. B.; Okamoto, H.; Subramanian, P. R.; Kacprzak, L. *Binary Alloy Phase Diagrams*; ASM International: Materials Park, OH, 1996. (c) Tripathi, S. N.; Bharadwaj, S. R.; Dharwadkar, S. R. *J. Phase Equilib.* **1993**, *14*, 638.

(2) Kusada, K.; Yamauchi, M.; Kobayashi, H.; Kitagawa, H.; Kubota, Y. *J. Am. Chem. Soc.* **2010**, *132*, 15897.

(3) (a) Papaconstantopoulos, D. A.; Klein, B. M.; Economou, E. N.; Boyer, L. L. *Phys. Rev. B* **1978**, *17*, 141. (b) Gelatt, C. D.; Ehrenreich, H.; Weiss, J. A. *Phys. Rev. B* **1978**, *17*, 1940. (c) Vuillemin, J. J.; Priestly, M. G. *Phys. Rev. Lett.* **1965**, *14*, 307. (d) Mueller, F. M.; Freeman, A. J.; Dimmock, J. O.; Furdyna, A. M. *Phys. Rev. B* **1984**, *1*, 4619. (e) Wicke, E. *J. Less-Common Met.* **1984**, *101*, 17.

(4) (a) Alefeld, G.; Völkl, J. *Hydrogen in Metals I*; Springer-Verlag: Berlin, 1978; p 108. (b) Alefeld, G.; Völkl, J. *Hydrogen in Metals II*; Springer-Verlag: Berlin, 1978; p 73.

(5) (a) Ke, X.; Kramer, G. J.; Løvvik, O. M. *J. Phys.: Condens. Matter* **2004**, *16*, 6267. (b) Flanagan, T. B.; Wang, D.; Noh, H. *J. Alloys Compd.* **1997**, *253−254*, 216. (c) Barlag, H.; Opara, L.; Züchner, H. *J. Alloys Compd.* **2002**, *330−332*, 434. (d) Sonwane, C. G.; Wilcox, J.; Ma, Y. H. *J. Phys. Chem. B* **2006**, *110*, 24549.

(6) (a) Cabrera, A. L.; Morales, E. L.; Hansen, J.; Schuller, K. *Appl. Phys. Lett.* **1995**, *66*, 1216. (b) Frölich, K.; Severin, H. G.; Hempelmann, R.; Wicke, E. *Z. Phys. Chem. (Muenchen, Ger.)* **1980**, *119*, 33. (c) Szafranski, A. W. *J. Phys.: Condens. Matter.* **2003**, *15*, 3583.

(7) (a) Perkas, N.; Teo, J.; Shen, S.; Wang, Z.; Highfield, J.; Zhong, Z.; Gedanken, A. *Phys. Chem. Chem. Phys.* **2011**, *13*, 15690. (b) Bowker, M. *Chem. Soc. Rev.* **2008**, *37*, 2204. (c) Grass, M. E.; Zhang, Y.; Butcher, D. R.; Park, J. Y.; Li, Y.; Bluhm, H.; Bratlie, K. M.; Zhang, T.; Somorjai, G. A. *Angew. Chem., Int. Ed.* **2008**, *47*, 8893. (d) Zhang, Y.; Grass, M. E.; Huang, W.; Somorjai, G. A. *Langmuir* **2010**, *26*, 16463. (e) Joo, S. H.; Park, J. K.; Renzas, J. R.; Butcher, D. R.; Huang, W.; Somorjai, G. A. *Nano Lett.* **2010**, *10*, 2709.

(8) Ertl, G. *Angew. Chem., Int. Ed.* **2008**, *47*, 3524.

(9) (a) Xiao, L.; Zhuang, L.; Liu, Y.; Lu, J.; Abruna, H. D. *J. Am. Chem. Soc.* **2009**, *131*, 602. (b) Newton, M. A.; Belver-Coldeira, C.; Martínez-Arias, A.; Fernández-García, M. *Nat. Mater.* **2007**, *6*, 528.

(10) Schultz, N. E.; Gherman, B. E.; Cramer, C. J.; Truhlar, D. G. *J. Phys. Chem. B* **2006**, *110*, 24030.

(11) (a) Lee, H. C.; Potapova, Y.; Lee, D. *J. Power Sources* **2012**, *216*, 256. (b) McFarland, E. *Science* **2012**, *338*, 340.

(12) (a) Beutl, M.; Lesnik, J. *Surf. Sci.* **2001**, *482−485*, 353. (b) Abdelsayed, V.; Aljarash, A.; El-Shall, M. S.; Othman, Z. A. A.; Alghamdi, A. H. *Chem. Mater.* **2009**, *21*, 2825. (c) Renzas, J. R.; Huang, W.; Zhang, Y.; Grass, M. E.; Hoang, D. T.; Alayoglu, S.; Butcher, D. R.; Tao, F.; Liu, Z.; Somorjai, G. A. *Phys. Chem. Chem. Phys.* **2011**, *13*, 2556.

(13) Nakamura, E.; Sato, K. *Nat. Mater.* **2011**, *10*, 158.

(14) (a) Kobayashi, H.; Yamauchi, M.; Kitagawa, H.; Kubota, Y.; Kato, K.; Takata, M. *J. Am. Chem. Soc.* **2010**, *132*, 5576. (b) Kakade, B. A.; Tamaki, T.; Ohashi, H.; Yamaguchi, T. *J. Phys. Chem. C* **2012**, *116*, 7464. (c) Kobayashi, H.; Morita, H.; Yamauchi, M.; Ikeda, R.; Kitagawa, H.; Kubota, Y.; Kato, M.; Takata, M.; Toh, S.; Matsumura, S. *J. Am. Chem. Soc.* **2012**, *134*, 12390. (d) Petkov, V.; Wanjala, B. N.; Loukrakpam, R.; Luo, J.; Yang, L.; Zhong, C.; Shastri, S. *Nano Lett.* **2012**, *12*, 4289. (e) Hernández-Fernández, P.; Rojas, S.; Ocón, P.; Gómez de la Fuente, J. L.; San Fabián, J.; Sanza, J.; Peña, M. A.; García-García, F. J.; Terreros, P.; Fierro, J. L. G. *J. Phys. Chem. C* **2007**, *111*, 2913. (f) Essinger-Hileman, E. R.; DeCicco, D.; Bondi, J. F.; Schaak, R. E. *J. Mater. Chem.* **2011**, *21*, 11599.

(15) Denton, A. R.; Ashcroft, N. W. *Phys. Rev. A* **1991**, *43*, 3161.

(16) (a) Ott, S. *Science* **2011**, *333*, 1714. (b) Farha, O. K.; Yazaydin, A. Ö.; Eryazici, I.; Malliakas, C. D.; Hauser, B. G.; Kanatzidis, M. G.; Nguyen, S. T.; Snurr, R. Q.; Hupp, J. T. *Nat. Chem.* **2010**, *2*, 944. (c) Hull, J. F.; Himeda, Y.; Wang, W.; Hashiguchi, B.; Periana, R.; Szalda, D. J.; Muckerman, J. T.; Fujita, E. *Nat. Chem.* **2012**, *4*, 383. (d) Doroodian, A.; Dengler, J. E.; Genest, A.; Rösch, N.; Rieger, B. *Angew. Chem., Int. Ed.* **2010**, *49*, 1871.

(17) Fukai, Y. *The Metal-Hydrogen System, Basic Bulk Properties*, 2nd ed.; Springer-Verlag: Berlin, 2005; p 9.

(18) Yamauchi, M.; Ikeda, R.; Kitagawa, H.; Takata, M. *J. Phys. Chem. C* **2008**, *112*, 3294.

(19) Xu, J.; White, T.; Li, P.; He, C.; Yu, J.; Yuan, W.; Han, Y. *J. Am. Chem. Soc.* **2010**, *132*, 10398.

(20) (a) Sandoval, A.; Aguilar, A.; Louis, C.; Traverse, A.; Zanella, R. *J. Catal.* **2011**, *281*, 40. (b) Wang, A.; Liu, J.; Lin, S. D.; Lin, T.; Mou, C. *J. Catal.* **2005**, *233*, 186.

(21) (a) Engel, T.; Ertl, G. *J. Chem. Phys.* **1978**, *69*, 1267. (b) Ladas, S.; Poppa, H.; Boudart, M. *Surf. Sci.* **1981**, *102*, 151. (c) Liu, K.; Wang, A.; Zhang, T. *ACS Catal.* **2012**, *2*, 1165.

(22) (a) Hammer, B.; Nørskov, J. K. *Nature* **1995**, *376*, 238. (b) Hammer, B.; Nørskov, J. K. *Surf. Sci.* **1995**, *343*, 211.

(23) Xu, J.; White, T.; Li, P.; He, C.; Yu, J.; Yuan, W.; Han, Y. F. *J. Am. Chem. Soc.* **2010**, *132*, 10398.

(24) Nikolla, E.; Schwank, J.; Linic, S. *J. Am. Chem. Soc.* **2009**, *131*, 2747.